Experimental X-Ray Ghost Imaging

Daniele Pelliccia,[1,2,3,*] Alexander Rack,[4] Mario Scheel,[5] Valentina Cantelli,[6,4] and David M. Paganin[3]
[1]*School of Science, RMIT University, Victoria 3001, Australia*
[2]*Australian Synchrotron, Victoria 3168, Australia*
[3]*School of Physics and Astronomy, Monash University, Victoria 3800, Australia*
[4]*European Synchrotron Radiation Facility, 38043 Grenoble, France*
[5]*Synchrotron Soleil, 91192 Gif-sur-Yvette, France*
[6]*Helmholtz-Zentrum Dresden-Rossendorf, 01328 Dresden, Germany*
(Received 16 May 2016; published 7 September 2016)

We report an experimental proof of principle for ghost imaging in the hard-x-ray energy range. We use a synchrotron x-ray beam that is split using a thin crystal in Laue diffraction geometry. With an ultrafast imaging camera, we are able to image x rays generated by isolated electron bunches. At this time scale, the shot noise of the synchrotron emission process is measurable as speckles, leading to speckle correlation between the two beams. The integrated transmitted intensity from a sample located in the first beam is correlated with the spatially resolved intensity measured in the second, empty, beam to retrieve the shadow of the sample. The demonstration of ghost imaging with hard x rays may open the way to protocols to reduce radiation damage in medical imaging and in nondestructive structural characterization using free electron lasers.

DOI: 10.1103/PhysRevLett.117.113902

Ghost imaging, in its basic form, is the technique of indirectly imaging a sample by using the correlation between the intensity recorded at two detectors illuminated by spatially separated correlated beams [1]. A bucket detector measures the total intensity transmitted (or scattered) by a sample, placed in one of the beams. The sample image is then retrieved by correlating the output of the bucket detector with a pixel array detector located in the other beam, namely, the one that has not directly interacted with the sample.

Initially demonstrated with entangled photon pairs [2], ghost imaging was subsequently performed using the correlation between classical coherent light beams [3]. The protocol was shown to be very robust, leading to experimental studies on ghost imaging using pseudothermal light [4–6], true thermal sources [7], and, eventually, computational ghost imaging [8], where a computer-controlled spatial light modulator generates a series of known illuminating fields, altogether removing the need for imaging the empty beam. Of relevance for this Letter is also a very recent demonstration of Fourier transform ghost imaging using speckle fields generated with partially coherent synchrotron x rays [9].

At the heart of thermal ghost imaging is the *speckle* correlation in the intensity fluctuations of the illuminating beam. The speckles can be produced either by near-field diffraction of a coherent beam by a slowly moving diffracting object [4–6,9] or by taking advantage of the natural fluctuations of true thermal light [7], as in the Hanbury Brown–Twiss (intensity) interferometer [10]. In this Letter we use the latter mechanism to produce the first proof of principle demonstration of hard-x-ray direct ghost imaging using synchrotron emission from an undulator in a third generation synchrotron storage ring.

Synchrotron emission from an ultrarelativistic electron bunch provides a natural thermal source of hard x rays. Intensity correlation x-ray experiments, proposed as far back as 1975 [11] (see also Ref. [12]), were employed several times for coherence characterization of synchrotron [13–15] and x-ray free electron laser (FEL) [16] beams. To date, though, x-ray speckle correlation has never been used for direct ghost imaging.

Such imaging applications are now feasible, given the availability of ultrafast hard-x-ray imaging cameras [17] that permit spatially resolved measurement with a single pulse. By using one such ultrafast detector, coupled to an image intensifier, the light emitted from a single electron bunch is sufficient to form an image containing natural speckles arising from the shot noise of the electron bunch. By splitting the beam into two spatially separated locations on the camera screen and placing an object in one of the beams, the ghost image of the object can be recovered by a suitable intensity correlation between the two speckle beams. Demonstrating ghost imaging with hard x rays is significant, mainly due to a striking peculiarity of the ghost imaging mechanism. Arising from the intensity correlation between separate beams, ghost imaging is remarkably insensitive to turbulence in either beam [18], and applications in atmospheric imaging have followed from this property. Turbulence is not a problem for hard-x-ray imaging, but radiation dose certainly is. The very same idea of robustness to turbulence could be used to make the counting statistics in the two beams very different. In other words, the beam that interacts with the sample could be

greatly attenuated (with increased associated noise), yet maintaining the intensity correlations with the second, much more intense beam. Therefore, forming ghost images with x rays that never interacted with a sample is an extremely interesting avenue for mitigating radiation damage. Consequences can be appreciated in medical imaging diagnostics, but also in biological x-ray microscopy, where radiation damage often represents the effective limit to the achievable resolution. Emerging applications of FELs for single molecule diffraction could also benefit from "diffraction without destruction" achieved via the ghost imaging mechanism [19].

Our ghost imaging experiment was carried out at the ID19 beam line of the European Synchrotron ESRF in Grenoble, France. We used a special operation mode of the storage ring, in which four equidistant electron bunches are stored, carrying a maximum current of 10 mA per bunch. In this way the temporal separation between the bunches is approximately 704 ns, corresponding to a frequency of about 1.42 MHz.

The experimental setup is depicted in Fig. 1. The beam from the undulator was focused by a Be refractive lens stack to a focal spot of approximately 1.5×1.1 mm ($H \times V$) at the beam splitter position. The monochromator—a pair of Si crystals located at 140 m from the source—monochromatized the beam at an energy of 20 keV. The beam splitter, constituted by a 300 μm thick Si crystal polished on both faces, was aligned to select one of the (220) Laue reflections in the forward direction. At the same time, the crystal enabled a portion of the undiffracted beam to be transmitted in the forward direction [20]. The camera was placed 20 cm downstream of the beam splitter to enable detection, within its field of view, of both diffracted and transmitted beams. The camera was a Photron FASTCAM SA-Z, coupled with a 200 μm thick phosphor screen scintillator (CsI:Na) and an image intensifier [21] with a P46 (YAG:Ce) phosphor screen.

Both the refractive lens stack and the image intensifier have been adopted to guarantee sufficient counting statistics to operate the camera at a nominal frame rate $f_c = 2.88$ MHz, more than twice the storage ring frequency, to ensure correct sampling. In reality, as we discovered during postprocessing, the actual frame rate of the camera was lower and was equal to 2.57 MHz. Consequences of this fact are discussed further below and in the Supplemental Material [22].

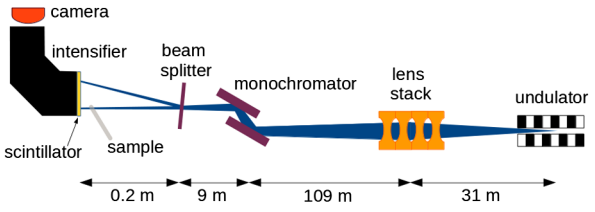

FIG. 1. Scheme of the experimental setup (not to scale). X-ray beam propagation is from right to left. X-ray pulses from the undulator are focused by a refractive lens stack and then monochromatized by a double-bounce Si monochromator. The beam splitter, working in Laue diffraction, is located at the focal position of the lenses. Both transmitted and diffracted beams are imaged on the ultrafast camera coupled with a scintillator and an image intensifier.

A typical frame recorded by the Photron camera is shown in Fig. 2(a). The object, a copper wire of 200 μm diameter was aligned approximately in the middle of the transmitted beam, which appears in the bottom right corner of Fig. 2(a). The diffracted beam does not contain the object and is used as a reference beam. Close-ups of the diffracted and transmitted beams are shown in Figs. 2(b) and 2(c), respectively. In this proof of principle experiment, the intensity of the transmitted beam was integrated over an area of 30×20 pixels around the beam center to reproduce the one-dimensional (time dependent) bucket signal. The ghost image $T_{\mathrm{GI}}(x, y)$ was then obtained by correlating the bucket signal B_r with the reference image $I_r(x, y)$ [23]:

$$T_{\mathrm{GI}}(x, y) = \langle (B_r - \langle B \rangle) I_r(x, y) \rangle, \tag{1}$$

where $\langle B \rangle$ is the average bucket signal and the averages are calculated over an ensemble of 20 000 frames. In order to retrieve the ghost image, however, Fourier filtering of both the bucket and reference signals had to be performed. Both signals are generated in a diffraction process and, due to vibrations of the beam splitter mounting, the reference and bucket beams display a low frequency anticorrelation; small changes in the angular position of the beam splitter

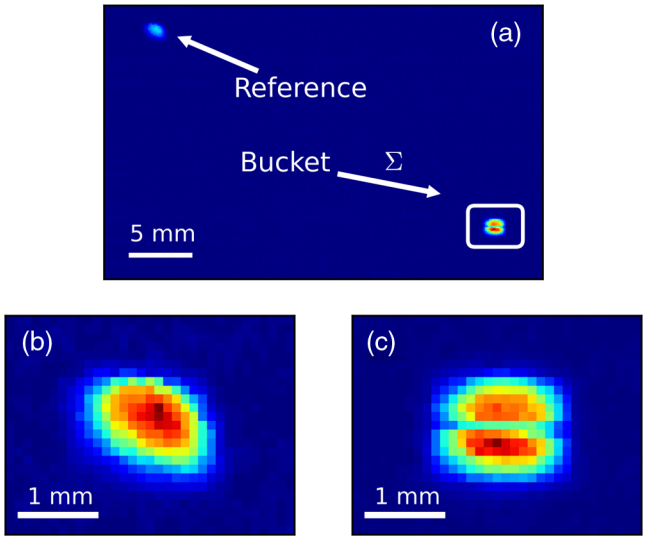

FIG. 2. Representative frame recorded by the Photron camera. (a) Complete frame with marked positions of the reference and bucket beams (the diffracted and transmitted beams, respectively). The shadow of the wire is visible in the bucket beam. The white frame marks the region that has been integrated over, to obtain the bucket signal B_r. (b),(c) Close-up views of the reference and bucket beams (with sample), respectively.

deviate intensity from the transmitted to the diffracted beam, and vice versa (see Fig. 1 in the Supplemental Material [22]).

Such low frequency components, visible in the power spectrum plotted in Fig. 3(a), must be filtered out to isolate the "true" speckle correlation arising from single bunch emission. We originally planned to window the component corresponding to the storage ring frequency f_r. However, because of the fact that the actual camera frame rate was $f_c < 2f_r$, the Nyquist frequency $f_N = f_c/2$ for the system was below the storage ring frequency. As a result, the storage ring frequency was not directly accessible, and only an alias at a frequency $f_c - f_r = 1.15$ MHz is visible in the power spectrum. The alias is outlined by the dashed box in Fig. 3(a). In addition, the power spectrum shows a second prominent peak at $f_{r/2} = 0.72$ MHz, corresponding to half of the storage ring frequency. Both peaks can be used for ghost imaging by selecting the frequency components of either the alias or $f_{r/2}$. This corresponds to selecting each x-ray pulse (albeit at down-shifted frequency) or the average of two pulses, respectively. In both cases the natural speckle pattern arising from the shot noise of the electron bunches becomes predominant, and it therefore produces the true random correlation needed for the ghost imaging. The image of the reference beam, before and after Fourier filtering, is shown in Fig. 2 in the Supplemental Material [22].

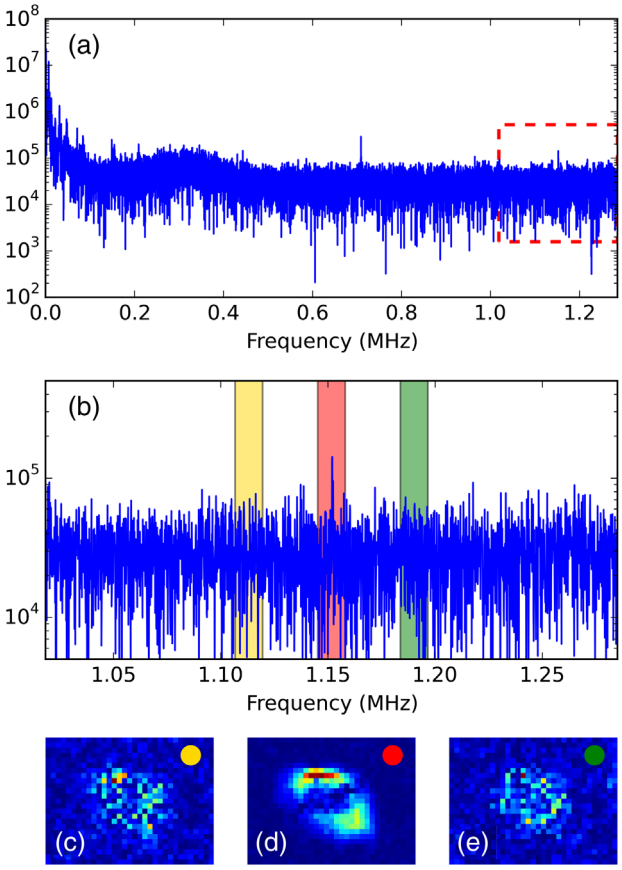

FIG. 3. The effect of Fourier filtering on the ghost image. (a) Power spectrum of the bucket signal. The low frequency components are related to mechanical instabilities of the crystals. The two sharp peaks visible at higher frequency correspond to half of the ring frequency (0.72 MHz) and the alias of the primary storage ring frequency at 1.15 MHz (see the text for details). The region marked by the dashed box is zoomed in in (b), where three different windows used for calculation are overlaid. (c)–(e) Ghost images obtained by Fourier filtering with the windows displayed in (b). Ghost imaging is obtained only when the window includes the alias of the storage ring frequency. Only in this case is a true correlation between the reference and the bucket beam present. The image size in (c)–(e) is 3.7×2.8 mm ($H \times V$).

Here, we show, as an example, the ghost imaging obtained by windowing the alias of the storage ring frequency at 1.15 MHz. A close-up view of the power spectrum around the alias position is plotted in Fig. 3(b). To demonstrate the use of the speckle correlation, we performed the windowing around three different frequencies, shown as shaded areas in Fig. 3(b). Green and gold areas correspond, respectively, to higher and lower frequencies of the 1.15 MHz peak. The ghost image, calculated according to Eq. (1) using the side windows, does not show any structure due to the lack of a physical intensity correlation between the two beams. On the contrary, by selecting the window around the alias of the storage ring frequency, the ghost image clearly displays an oblique shadow. That shadow is the ghost image of the wire, deformed according to the affine transform that relates the shape of the diffracted beam to the incident beam shape.

As a further verification of the mechanism, we repeated the experiment after moving the wire in the diffracted beam, i.e., by exchanging the role of the bucket and reference signals. The same data analysis procedure—windowing the alias peak—before ensemble averaging generates the ghost image shown in Fig. 4. Figures 4(a) and 4(c) represent the image obtained when windowing just below or above the alias frequency 1.15 MHz. Figure 4(b) is the image obtained when the window contains the alias frequency.

Two important differences between this image and the one in Fig. 3(d) are observable. The first difference originates from the position of the bucket beam. In this

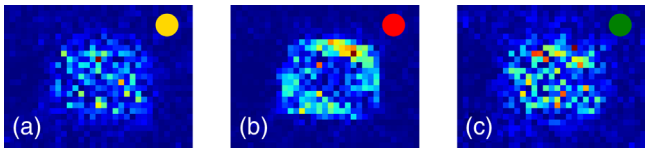

FIG. 4. Ghost imaging obtained by exchanging the role of the reference and the bucket. The transmitted beam is now the reference and the wire is moved to the diffracted beam, whose intensity distribution is integrated over an area of 20×30 pixels. The same Fourier filtering procedure described in Fig. 3 is applied here and the results are displayed in (a)–(c). (b) corresponds to selecting the window (red) centered on the alias frequency. The image size in all panels is 3.7×2.8 mm ($H \times V$).

second case, the position of the bucket beam is variable due to the mechanical vibrations of the crystal discussed before. As a consequence, the sample is illuminated by a variable beam and the ghost image in Fig. 4(b) appears to be noisier than the corresponding image in Fig. 3(d). This problem is not present in the first case, as the position of the transmitted beam is not affected by mechanical vibrations of the crystal.

The second difference is in the orientation of the ghost image. Having switched the role of the bucket and reference beams, the affine transformation relating the ghost image to the actual sample image is inverted. Hence, the apparent orientation of the wire in Fig. 4(b) is the opposite of that in Fig. 3(d).

A final remark concerns the robustness of the ghost imaging mechanism studied here. In the ideal situation, each speckle image acquired in a single frame must be generated with the x rays produced from a single electron bunch. In practice, however, this is not strictly required. Some degree of mixing between the x rays emitted by different pulses is acceptable, as long as the speckle visibility is not washed out. The sum of two (or a few) speckle images is still a speckle image, and therefore ghost images can still be retrieved. For instance, as mentioned before, we successfully retrieved a ghost image by windowing the $f_{r/2}$ peak at 0.72 MHz, corresponding to considering the weighted average of two consecutive pulses. The image can be found in Fig. 3 of the Supplemental Material [22].

Regardless of the camera frame rate, light mixing between pulses occurs as a consequence of both the electronic noise in detection and the scintillator's afterglow. X rays are indirectly detected by scintillator screens [24]. The process of scintillation has a characteristic decay time which is, in general, much longer than the duration of a single x-ray pulse; in fact, it can be of the same order as the time separation between two consecutive pulses. The primary decay constants of the scintillation process for the scintillator we used were 630 and 70 ns for the CsI:Na and the YAG:Ce, respectively (see Fig. 4 in the Supplemental Material [22]). Therefore, even if the timing of the camera is adequate to select individual pulses, the image of a single pulse always contains residual intensity from the previous pulses, plus a constant background due to electronic noise. The background contribution, however, is filtered out during the Fourier processing, which eliminates all frequencies outside the selected window, and therefore does not contribute to the ghost imaging reconstruction procedure. The residual mixing between consecutive pulses is therefore purely limited to the speckle contribution.

In conclusion, we reported the experimental demonstration of direct ghost imaging using hard x rays. The protocol was enabled by detecting the natural speckles present in the x-ray emission from a single electron bunch traveling in an undulator. A beam splitter was used to generate two copies of the beam, and both copies were simultaneously detected by a high speed camera. The camera frame rate was high enough to nearly isolate the x rays from a single bunch or the average of two consecutive bunches. The sample (an x-ray opaque Cu wire) was placed in one of the beams, whose image was spatially integrated to constitute a point (bucket) detector. The ghost image of the wire was recovered under two configurations, using the intensity correlation between the bucket signal and the image of the empty beam.

The experimental demonstration of direct x-ray ghost imaging is extremely interesting for potential applications in medical imaging and ultrafast x-ray studies using free electron lasers. In both cases, ghost imaging may represent an avenue to reduce the radiation dose on the sample by using a suitably weak bucket beam and maintaining the speckle correlation with the reference beam.

The authors gratefully acknowledge M. Rutherford (Imperial College London) and Photron UK for kindly lending us the Photron camera used in this experiment. M. S. acknowledges the support of the French National Research Agency (ANR) via EQUIPEX Grant No. ANR-11-EQPX-0031.

*daniele.pelliccia@rmit.edu.au

[1] B. I. Erkmen and J. H. Shapiro, Ghost imaging: from quantum to classical to computational, Adv. Opt. Photonics **2**, 405 (2010).
[2] T. B. Pittman, Y. H. Shih, D. V. Strekalov, and A. V. Sergienko, Optical imaging by means of two-photon quantum entanglement, Phys. Rev. A **52**, R3429 (1995).
[3] R. S. Bennink, S. J. Bentley, and R. W. Boyd, "Two-Photon" Coincidence Imaging with a Classical Source, Phys. Rev. Lett. **89**, 113601 (2002).
[4] A. Gatti, E. Brambilla, M. Bache, and L. A. Lugiato, Ghost Imaging with Thermal Light: Comparing Entanglement and Classical Correlation, Phys. Rev. Lett. **93**, 093602 (2004).
[5] Y. Cai and S.-Y. Zhu, Ghost imaging with incoherent and partially coherent light radiation, Phys. Rev. E **71**, 056607 (2005).
[6] A. Valencia, G. Scarcelli, M. D'Angelo, and Y. H. Shih, Two-Photon Imaging with Thermal Light, Phys. Rev. Lett. **94**, 063601 (2005).
[7] D. Zhang, Y. H. Zhai, L. A. Wu, and X. H. Chen, Correlated two-photon imaging with true thermal light, Opt. Lett. **30**, 2354 (2005).
[8] J. H. Shapiro, Computational ghost imaging, Phys. Rev. A **78**, 061802(R) (2008).
[9] H. Yu, R. Lu, S. Han, H. Xie, G. Du, T. Xiao, and D. Zhu, preceding Letter, Fourier-Transform Ghost Imaging with Hard X Rays, Phys. Rev. Lett. **117**, 113901 (2016).
[10] R. Hanbury Brown and R. Q. Twiss, Correlation between photons in two coherent beams of light, Nature (London) **177**, 27 (1956).
[11] E. V. Shuryak, Two-photon correlations in synchrotron radiation as a method of studying the beam, Sov. Phys. JETP **40**, 30 (1975).

[12] E. Ikonen, Interference Effects between Independent Gamma Rays, Phys. Rev. Lett. **68**, 2759 (1992).
[13] E. Gluskin, I. McNulty, P. J. Viccaro, and M. R. Howells, X-ray intensity interferometer for undulator radiation, Nucl. Instrum. Methods Phys. Res., Sect. A **319**, 213 (1992).
[14] M. Yabashi, K. Tamasaku, and T. Ishikawa, Characterization of the Transverse Coherence of Hard Synchrotron Radiation by Intensity Interferometry, Phys. Rev. Lett. **87**, 140801 (2001).
[15] A. Singer, U. Lorenz, A. Marras, A. Klyuev, J. Becker, K. Schlage, P. Skopintsev, O. Gorobtsov, A. Shabalin, H. C. Wille, H. Franz, H. Graafsma, and I. A. Vartanyants, Intensity Interferometry of Single X-Ray Pulses from a Synchrotron Storage Ring, Phys. Rev. Lett. **113**, 064801 (2014).
[16] A. Singer, U. Lorenz, F. Sorgenfrei, N. Gerasimova, J. Gulden, O. M. Yefanov, R. P. Kurta, A. Shabalin, R. Dronyak, R. Treusch, V. Kocharyan, E. Weckert, W. Wurth, and I. A. Vartanyants, Hanbury Brown–Twiss Interferometry at a Free-Electron Laser, Phys. Rev. Lett. **111**, 034802 (2013).
[17] A. Rack, M. Scheel, and A. N. Danilewsky, Real-time direct and diffraction X-ray imaging of irregular silicon wafer breakage, Int. Union Crystallogr. J. **3**, 108 (2016).
[18] R. E. Meyers, K. S. Deacon, and Y. Shih, Turbulence-free ghost imaging, Appl. Phys. Lett. **98**, 111115 (2011).
[19] Z. Li, N. Medvedev, H. Chapman, and Y. Shih, Radiation damage free x-ray ghost diffraction with atomic resolution, arXiv:1511.05068.
[20] U. Bonse and M. Hart, An x-ray interferometer, Appl. Phys. Lett. **6**, 155 (1965).
[21] C. Ponchut, Evaluation of an X-ray imaging detector based on a CMOS camera with logarithmic response, Nucl. Instrum. Methods Phys. Res., Sect. A **457**, 270 (2001).
[22] See Supplemental Material at http://link.aps.org/supplemental/10.1103/PhysRevLett.117.113902 for a discussion on the Fourier analysis of the time-dependent signals and the experimental ghost imaging obtained with the $f_{r/2}$ peak.
[23] O. Katz, Y. Bromberg, and Y. Silberberg, Compressive ghost imaging, Appl. Phys. Lett. **95**, 131110 (2009).
[24] P. A. Rodnyi, *Physical Processes in Inorganic Scintillators* (CRC Press, Boca Raton, 1997).